Vortex matching at 6 T in YBa$_2$Cu$_3$O$_{7-\delta}$ thin films by imprinting a 20-nm periodic pinning array with a focused helium-ion beam

Max Karrer,[1] Bernd Aichner,[2] Katja Wurster,[1] César Magén,[3] Christoph Schmid,[1] Robin Hutt,[1] Barbora Budinská,[2,4] Oleksandr V. Dobrovolskiy,[2,5] Reinhold Kleiner,[1] Wolfgang Lang,[2,*] Edward Goldobin,[1] and Dieter Koelle[1,†]

[1]*Physikalisches Institut, Center for Quantum Science (CQ) and LISA$^+$, University of Tübingen, Auf der Morgenstelle 14, 72076 Tübingen, Germany*

[2]*Faculty of Physics, University of Vienna, Boltzmanngasse 5, 1090 Vienna, Austria*

[3]*Instituto de Nanociencia y Materiales de Aragón (INMA), CSIC-Universidad de Zaragoza, 50009 Zaragoza, Spain*

[4]*Vienna Doctoral School in Physics, University of Vienna, Boltzmanngasse 5, 1090 Vienna, Austria*

[5]*Cryogenic Quantum Electronics, Institut für Elektrische Messtechnik und Grundlagen der Elektrotechnik, Technische Universität Braunschweig, Hans-Sommer-Str. 66, 38106 Braunschweig, Germany and Laboratory for Emerging Nanometrology, Technische Universität Braunschweig, Langer Kamp 6a/b, 38106 Braunschweig, Germany*

Controlled engineering of vortex pinning sites in copper-oxide superconductors is a critical issue in manufacturing devices based on magnetic flux quanta. To address this, we employed a focused He-ion beam (He-FIB) to irradiate thin YBa$_2$Cu$_3$O$_{7-\delta}$ films and create ultradense hexagonal arrays of defects with lattice spacings as small as 20 nm. Critical current and magnetoresistance measurements demonstrate efficient pinning by a matching field of 6 T visible in a huge temperature range from the critical temperature T_c down to 2 K. These results show that He-FIB irradiation provides excellent opportunities for the development and application of superconducting fluxonic devices based on Abrikosov vortices. In particular, our findings suggest that such devices can operate at temperatures far below T_c, where superconductivity is robust.

I. INTRODUCTION

Superconductivity is a macroscopic quantum phenomenon characterized by the long-range coherence of charge carriers that make up the superconducting condensate. Most technically viable superconductors, including copper-oxide superconductors (HTS) with high critical temperature T_c, belong to the class of type-II superconductors. These materials allow the magnetic field to penetrate in the form of Abrikosov vortices of supercurrent, which carry the quantized magnetic flux $\Phi_0 = h/(2e)$, where h is Planck's constant and e is the elementary charge.

The properties and the interaction of Abrikosov vortices are controlled by two characteristic lengths: the Ginzburg-Landau coherence length ξ and the London penetration depth λ [1]. In the vortex center, the superconducting order parameter is suppressed to zero on the length scale ξ, thus creating a normal-conducting vortex core of approximately 2ξ diameter. As the formation of this normal-conducting core (i.e., the suppression of superconductivity) requires energy, the vortex will be preferentially pinned to a non-superconducting defect.

The magnetic field and the supercurrents circulating around the vortex core decay exponentially on a characteristic scale given by the London penetration depth $\lambda > \xi$, which determines the magnetic vortex-vortex interaction range. For thin superconducting films with thickness $t_z \lesssim \lambda$, the so-called Pearl length [2] $\Lambda = 2\lambda^2/t_z$ replaces λ.

Importantly, Ginzburg–Landau theory predicts the temperature dependence $\xi(T) = \xi(0)(1 - T/T_c)^{-1/2}$, which implies that $\xi(T) \to \infty$ at temperature $T \to T_c$. The same temperature dependence is predicted for $\lambda(T)$ [1]. Consequently, at temperatures near T_c, the size of the

*Contact author: wolfgang.lang@univie.ac.at
†Contact author: koelle@uni-tuebingen.de

vortex cores and their interaction range rises significantly. For the anisotropic compound $YBa_2Cu_3O_{7-\delta}$ (YBCO) used here as a prototypical HTS, the in-plane parameters are $\xi_{ab}(0) \approx 1.2$ nm and $\lambda_{ab}(0) \approx 250$ nm (for epitaxial thin films) [3–5].

A single Abrikosov vortex can store a classical data bit [6] and can be manipulated by several methods [7]. Vortices and interacting vortex ensembles have been suggested to build superconducting devices like vortex ratchets [8], cellular automata [9,10], superconducting diodes, vortex-based memory cells [11], and artificial vortex ice [12]. Although some of these concepts have been realized in experiments [13–15], it has not yet been possible to exploit the fundamentally possible degree of complexity and miniaturization. Hence, previous experiments with artificial vortex pinning sites were restricted by the employed etching techniques and had to be operated at temperatures $T \to T_c$ where the interaction length $\Lambda(T)$ is longer than the spacing a between the pins [16–18]. Innovative concepts, such as growing Nb films on nanopore templates [19], have been employed to mitigate these issues.

However, one aims to create devices that work at temperatures below about $T_c/2$ where superconductivity is robust and thermodynamic fluctuations do not reduce the collective vortex effects. Accordingly, the goal is to design and fabricate arrangements of many pinning sites in YBCO with diameters $d \gtrsim 2\xi_{ab}(T_c/2)$ and spacings a such that $d < a \ll \Lambda(T_c/2)$.

Thin films of YBCO are usually patterned by etching away material, which leads to a landscape with varying thickness. This process is extremely delicate and becomes even more challenging for nanoscale patterning due to the potential loss of oxygen through the open side faces of the remaining material. However, the loss of oxygen ultimately results in the degradation of the superconducting properties.

To overcome this issue, a masked light-ion beam from an implanter has been employed to fabricate regions with suppressed superconductivity [20–28]. The impacting ions create mainly Frenkel defects of the oxygen atoms in the YBCO crystal [29], while maintaining the crystallographic framework and the surface of the film intact. The binding energies are typically in the range of 1–3 eV [30,31] for O atoms in the CuO chains and about 8 eV [31] for the O atoms in the CuO_2 planes of YBCO. Point defects caused by ion impact break the superconducting carrier pairs and suppress T_c. These defects also scatter charge carriers and increase the normal-state resistivity. He^+ ions with moderate energy are ideal [32] for creating enough point defects to completely suppress superconductivity at a practically available fluence of $\phi < 10^{16}$ ions/cm^2 while still penetrating a YBCO film with a thickness less than about 100 nm [33]. However, columns of nonsuperconducting material of diameters [15] d and spacings [34] a

achieved by masked ion irradiation of YBCO are presently limited to $d \sim 70$ nm and $a \sim 100$ nm.

In this work, we utilize the focused He-ion beam (He-FIB) of a helium ion microscope (HIM) to achieve a spatial resolution well below 70 nm. We exemplify the advantages of the HIM's unique properties [35] by showcasing vortex-matching effects in a set of hexagonal pinning arrays. The matching effects show up in measurements of the critical current I_c and resistance R versus magnetic field B, and they are remarkably robust, extending to B as high as 6 T, and persisting at T from T_c down to 2 K. Our results represent a significant advancement in the fabrication of vortex pinning landscapes in thin YBCO films.

II. EXPERIMENTAL METHODS

A. Sample fabrication

For the studies presented here, thin YBCO films were grown epitaxially on (100)-oriented single crystal $(LaAlO_3)_{0.3}(Sr_2AlTaO_6)_{0.7}$ (LSAT) substrates by pulsed laser deposition . A 20-nm-thick Au film was deposited *in situ* by electron beam evaporation right after YBCO film growth, which serves for electrical contacting. The film thicknesses (see Table I) are small enough to permit complete penetration of the He-FIB. This guarantees a low level of angular and energy dispersion in the columnar defect (CD) array, a necessary condition for observing matching effects [36]. An excellent *c*-axis orientation of the films is confirmed by X-ray diffraction . Figure 1(a) shows a θ–2θ scan of the 37-nm-thick YBCO film, and the inset shows the rocking curve (ω scan) of the YBCO (005) peak with a full width at half maximum (FWHM) of 0.08°.

To fabricate microbridges on each chip, we used a combination of photolithography and Ar ion milling to pattern the Au/YBCO bilayer. Subsequently, the Au layer was removed with Lugol's iodine from the YBCO bridge structures to be exposed to He-FIB irradiation. The superconducting properties of the YBCO films did not change after patterning into microbridges. An optical image of a microbridge with an illustration of the electrical connections is shown in Fig. 1(b). The dimensions of different bridges are chosen to maintain the same number of irradiated dots for various pinning site spacings and to minimize the irradiation time for the denser lattices (see Table I).

B. He-FIB irradiation

The He-FIB irradiation was performed in a HIM (Zeiss Orion NanoFab) at the University of Tübingen. The sample chips were attached to aluminum sample stubs and grounded with silver paste. After mounting in the HIM, they were thermally acclimated for roughly 60 min before the irradiation procedure began. For simplicity, we will refer to the number of ions hitting a certain spot on the surface of the sample as the "dose" D, which will be
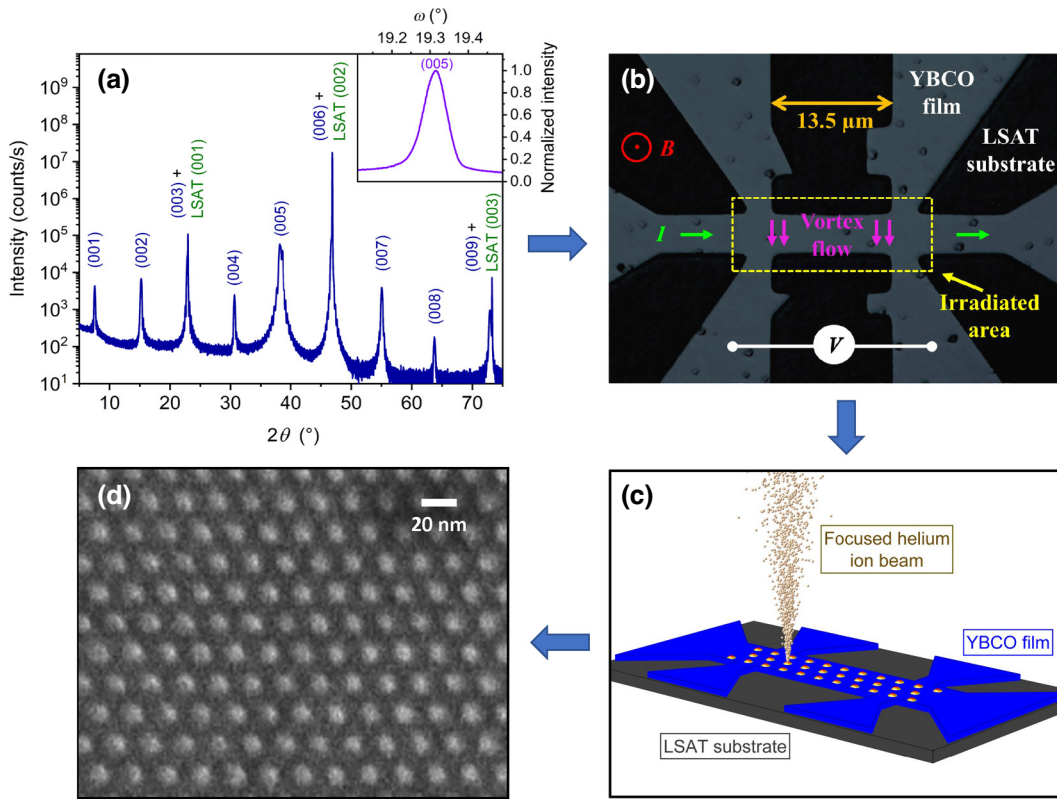
FIG. 1.   Fabrication of nanopatterns by He-FIB, (a) X-ray diffraction θ–2θ scan of the YBCO film before patterning (to create bridge H20); inset shows an ω scan of the (005) peak. (b) Optical micrograph of the bridge H20 with electrical connections after He-FIB irradiation within the area depicted by the yellow rectangle. (c) Sketch of the He-FIB patterning process. (d) Secondary electron helium ion microscope (HIM) image of a reference sample with a hexagonal $a = 20$ nm array after irradiation with an excessive dose $D = 60$ ki/dot. The white spots are blister-forming amorphous regions.

given in units of 1000 ions per dot (ki/dot). In Fig. 1(c), the fabrication of a hexagonal array of CDs by He-FIB is illustrated.

Notably, the dose $D = 10$ ki/dot was carefully selected to induce point defects and locally suppress T_c in the YBCO film, while avoiding amorphization within the CDs. To achieve this, the dose must not exceed a critical amorphization dose $D_c \approx 13$ ki/dot (see Sec. IV A 1). However, if $D < D_c$, the areas subjected to irradiation do not exhibit any visible surface degradation and cannot be seen by HIM imaging. To monitor the CD array fabrication process and visualize it, an auxiliary sample [shown in Fig. 1(d)] was

irradiated with a dose $D \gg D_c$. The scanning transmission electron microscopy (STEM) study presented in Sec. IV A 1 reveals that, for He-FIB doses above the amorphization threshold, the amorphous region causes local swelling, resulting in a bulge of the surface, as shown in Fig. 1(d).

Apart from the number of impinging ions, the lateral intensity profile of the He ion beam is also crucial. For our typical HIM parameters [a spot control (SC) value of 5 and an aperture of 10 µm], we assume a Gaussian intensity profile with an estimated FWHM beam diameter $\varnothing \sim 9$ nm. The SC value for a given aperture diameter determines the width of the beam diameter. A higher SC value produces

TABLE I.   Parameters of YBCO microbridges with pinning arrays reported in this paper. The length indicates the distance between the voltage probes. The critical temperature T_c is determined as the resistive transition's inflection point. The first magnetic matching field B_1 is calculated from Eq. (1) and confirmed by $I_c(B)$ and $R(B)$ measurements.

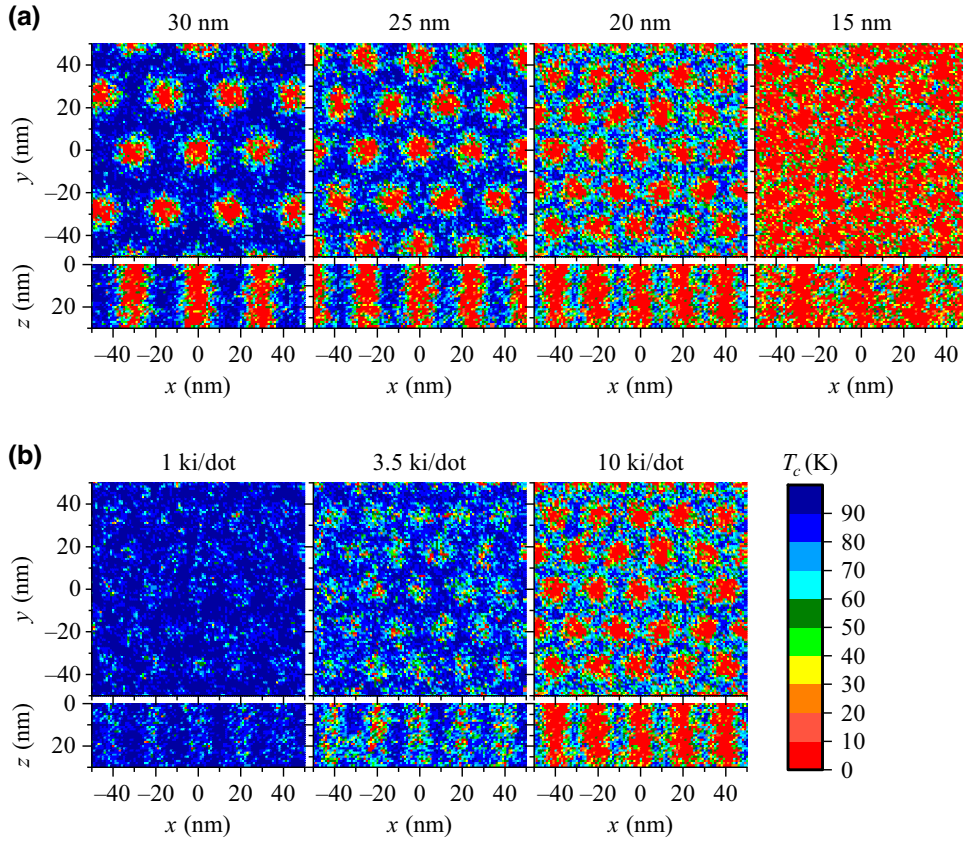| Name	Width (µm)	Length (µm)	Thickness (nm)	a (nm)	D (ki/dot)	T_c (K)	B_1 (T)
H30	8.0	20.0	26 ± 1	30 ± 0.6	10	75	2.7
H25	6.5	17.0	26 ± 1	25 ± 0.5	10	63	3.8
H20	5.0	13.5	37 ± 2	20 ± 0.5	10	52	6.0
H15	4.0	10.0	26 ± 1	15 ± 0.4	10	n/a	(10.6)

(a)

(b)

FIG. 2. Monte Carlo simulations of T_c suppression induced by He-FIB irradiation (with $\varnothing = 9$ nm) of YBCO; only the central parts of larger hexagonal patterns are shown. The x-y plots show cuts at $z = 15$ nm depth below the film surface, while the x-z plots show cuts at $y = 0$ nm. (a) Columnar defect (CD) lattices with various lattice spacings; $D = 10$ ki/dot. (b) CD lattices with $a = 20$ nm and various D.

a narrower beam profile at the expense of lower ion fluence and therefore longer irradiation time. For example, a narrow beam is required to draw lines across a YBCO microbridge to create Josephson junctions [37,38]. On the other hand, a lower SC value widens the beam and can lead to unwanted defects in the inter-CD areas, as discussed in Sec. IV A 2.

Throughout this work, we used a He-FIB with an energy of 30 keV. The irradiated area is limited by the field of view (FoV) of the HIM, and for optimum resolution of the HIM's beam deflection circuitry, the FoV should be $30 \times 30 \, \mu m^2$ or smaller. This provides a beam positioning accuracy of approximately 0.5 nm.

Several hexagonal arrays have been produced with spacings $a = 30, 25, 20, 15$ nm and doses ranging from $D = 1$ to 10 ki/dot. The different values of a were chosen to test the ultimate resolution that can be achieved. Here, we present the results for $D = 10$ ki/dot, which demonstrates the strongest pinning.

C. Transport measurements

The electrical measurements were carried out in a physical properties measurement system equipped with a 9-T superconducting solenoid and a variable temperature insert with a Cernox resistor for in-field temperature control (Quantum Design). For all experiments, the magnetic field was oriented perpendicular to the sample surface

(x-y plane), that is, the field is along the z axis. To rule out thermoelectric signals, resistance measurements were taken with constant excitation currents of 1.2–2.4 μA in both polarities. The magnetic field was swept in both polarities at fixed temperatures, and perfect mirror symmetry was observed. Furthermore, the results are independent of the magnetic field sweep direction and no hysteresis [26] was observed.

The critical current I_c is determined from isothermal voltage V versus current I measurements using a voltage criterion of 135 nV, which is above the noise floor of 40 nV and corresponds to an electric field $E = 100 \, \mu V/cm$. Supplementary resistance measurements in magnetic fields up to 12.5 T were performed in an Oxford Instruments helium bath cryostat.

III. SIMULATIONS

Our experiments were preceded by simulations of the expected $T_c(x, y, z)$ suppression patterns, which are summarized in Fig. 2. Briefly, atom displacement cascades due to He-FIB irradiation were calculated using the SRIM/TRIM program [39]. Individual He^+ atom impact points were shifted to simulate the Gaussian beam intensity distribution and the hexagonal irradiation pattern. The resulting three-dimensional landscapes of defects can be converted to local T_c values by using experimental data from uniformly large-area-irradiated thin YBCO films as
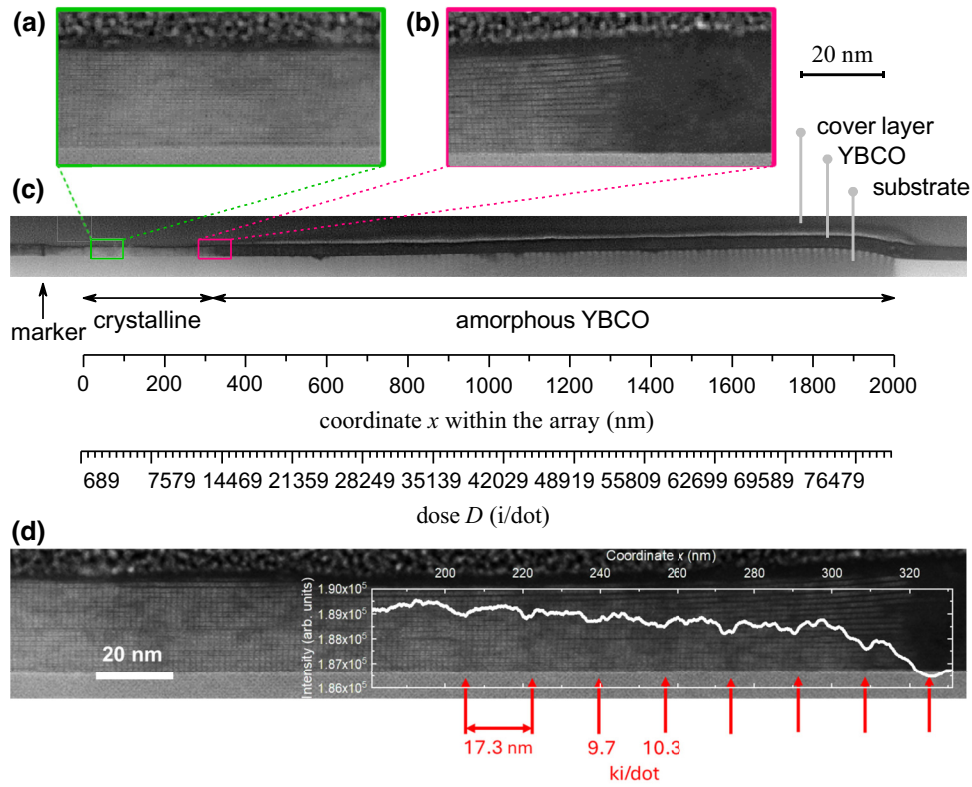
FIG. 3.   Cross-sectional High-angle annular dark field STEM image of the lamella extracted from a hexagonal array of CDs with the lattice constant $a = 20$ nm, length 2000 nm in the x-direction. The array has a dose gradient along the x axis given by $D(x) = 689$ i/dot $\cdot (N + 1) = 689$ i/dot $\cdot (1 + x/a')$, where $N = 0, \ldots, 115$ is the CD column number in the gradient direction and $a' = \sqrt{3}/2a \approx 17.32$ nm is the distance between the CDs in the x (D gradient) direction. (a),(b) Zoomed images in the region with preserved crystal structure and in the region with onset of amorphization ($x_c \approx 320$ nm, $D_c \approx 13$ ki/dot). (c) Overall view of the entire array. The scales below the image show the coordinate x within the array and the corresponding dose $D(x)$. Each small tick on the D axis corresponds to a position of a defect column (i.e., the distance between the ticks is a'). (d) The intensity profile (white) overlaid onto a selected part of the lamella's STEM image shows a slight contrast modulation with the periodicity a'. The red arrows indicate the locations of the irradiated spots.

calibration [40]. The size of the simulation cells is $1 \times 1 \times 1$ nm^3, similar to the in-plane and larger than the out-of-plane coherence lengths of YBCO.

In Fig. 2(a), the red dots indicate hexagonal arrays of well-formed nanocolumns with suppressed T_c. They are well separated down to $a = 20$ nm, leaving a superconducting matrix in between. Because of the straggling of the ion trajectories, these inter-CD regions have a finite but smaller defect density and hence also slightly reduced T_c values. In contrast, the simulation of an array with $a = 15$ nm reveals little T_c contrast between defect columns and inter-CD regions, making the observation of matching effects unlikely.

Furthermore, proper dose selection is crucial, as demonstrated in Fig. 2(b) for a lattice with spacings $a = 20$ nm. Doses of $D \ll 10$ ki/dot do not entirely suppress superconductivity. They only decrease T_c locally, resulting in a weaker pinning potential, as shown in Fig. 4(a). Conversely, doses $D > 10$ ki/dot provide no additional benefit since the suppression of T_c is already maximal.

On the contrary, an excessive number of defects causes crystal lattice instabilities, which spread into neighboring regions and widen the defect columns.

IV. RESULTS AND DISCUSSION

A. Optimization of irradiation parameters

1. Irradiation dose

To maintain the crystalline framework of YBCO and still suppress its superconductivity, it is essential to determine the optimal number of 30 keV He$^+$ ions (referred to as dose D) to irradiate one dot of the pinning lattice. If the dose exceeds the threshold value D_c, it causes the breakdown of the crystalline structure, making the YBCO film amorphous. To identify D_c, a hexagonal array of dots was used with a distance of $a = 20$ nm. The dots were irradiated with increasing doses in steps of 689 i/dot from row to row, linearly from 0.689 ki/dot to 80 ki/dot, leaving the other irradiation parameters the same as for sample H20.
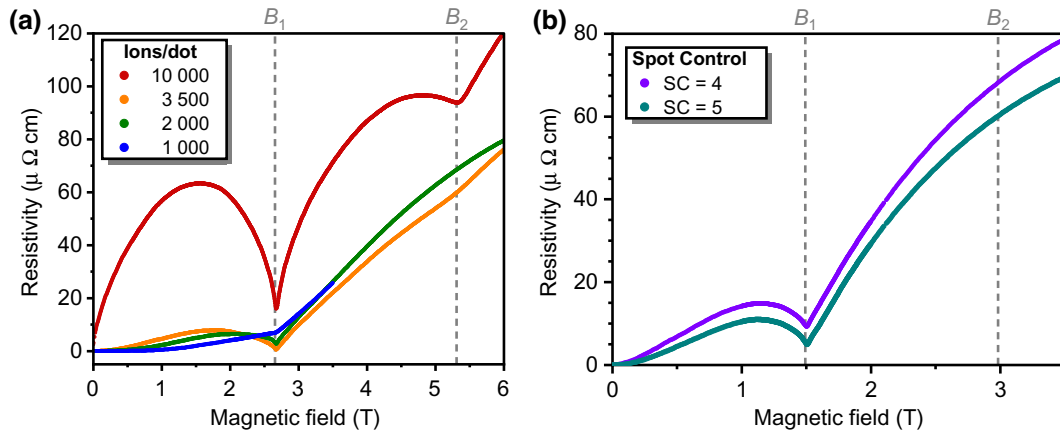
FIG. 4. Vortex-matching effects in the resistivity versus field curves of irradiated YBCO bridges. (a) Magnetoresistivity of four samples at $T/T_c \sim 0.96$ after irradiation with an $a = 30$ nm hexagonal pattern using SC = 4, and doses from 1 to 10 ki/dot. (b) Comparison of different spot control (SC) settings of the HIM. Two hexagonal pinning arrays with $a = 40$ nm were prepared with a dose $D = 2.0$ ki/dot on the same substrate. The magnetoresistivity at 86.5 K ($T/T_c \sim 0.96$) is plotted for SC = 4 and 5.

This array was characterized by aberration-corrected STEM in a probe-corrected FEI Titan 60-300 operated at 300 kV, equipped with a CEOS corrector for the condenser system, which provides a probe size below 1 Å. A high-angle annular dark field in STEM was used to provide Z-contrast images. The cross-sectional specimen was prepared by Ga$^+$-FIB in an FEI Helios 650 Dual Beam FIB system. The bright bubble-like contrast on top of the YBCO film in Figs. 3(a) and 3(b) is the Pt-C deposit grown by focused electron beam induced deposition to protect the YBCO film during transmission electron microscopy (TEM) lamella preparation in SEM-FIB equipment. This is a standard procedure with negligible impact on the film quality due to the low dose and low energy of the electron beam used. The same type of coverage is used in the highly crystalline pristine areas, which does not evidence any apparent amorphization or beam damage.

The cross-sectional STEM image of the entire irradiated region is shown in Fig. 3(c). At low doses, the crystalline structure of YBCO is preserved, as can be seen in the magnified detail depicted in Fig. 3(a). At a critical dose, $D_c \approx 13$ ki/dot, the crystalline structure of YBCO disappears in the STEM image, indicating the amorphization of the film, as displayed in Fig. 3(b). Note that at $D \lesssim D_c$, the YBCO layer already begins to swell, but the surface of the substrate remains flat. Only at substantially higher D is the substrate also damaged, and individual beam tracks become clearly visible on the right in Fig. 3(c). This observation proves that the reported vortex-matching effects are not caused by local strain from the substrate, but rather originate from subtle modifications of the YBCO structure.

The intensity profile for $D \lesssim D_c$ shown as an overlay to the STEM image in Fig. 3(d) reveals a reduction with increasing x (i.e., increasing D) that begins when the YBCO lattice expands and reaches its lowest value in the amorphized region. Intriguingly, it can clearly be seen that for $D < D_c$, the layered structure of YBCO is conserved, yet the intensity profile shows little dips with a periodicity of $a' = \sqrt{3}/2a$. Such an intensity depression is probably caused by the enhanced disorder in the CD channels. The width of the dips is up to 10 nm, supporting our previous estimate for the diameter of the CDs.

For lower dose values that do not cause visible damage, no signatures of the irradiation are visible in STEM images. However, the CDs created with lower doses strongly influence the behavior of magnetic flux quanta, as seen in electric transport measurements. The observation of magnetic-field commensurability effects with the flux-line lattice is a direct probe of efficient vortex pinning in periodic pinning landscapes. Minima of the resistivity and maxima of the critical current appear at so-called matching fields

$$B_k = k\Phi_0/A, \qquad (1)$$

where k is an integer or rational number of vortices contained within the unit cell of the hexagonal pinning array with area $A = \frac{\sqrt{3}}{2}a^2$. The field B_1 corresponds to the flux density of one vortex per pinning site. When the magnetic field $B > B_1$, one of two scenarios may occur: either some or all CDs are filled with multiquanta vortices when the CD radius is larger than the (in-plane) coherence length or interstitial vortices enter between the CDs [41].

The question of how lower doses $D \ll D_c$ influence the efficiency of the pinning lattices was investigated in several microbridges prepared on the same substrate. The bridges were patterned with a hexagonal $a = 30$ nm CD lattice using different doses but otherwise identical conditions. Figure 4(a) shows the resistivity ρ versus the applied magnetic field B of these bridges. Because T_c
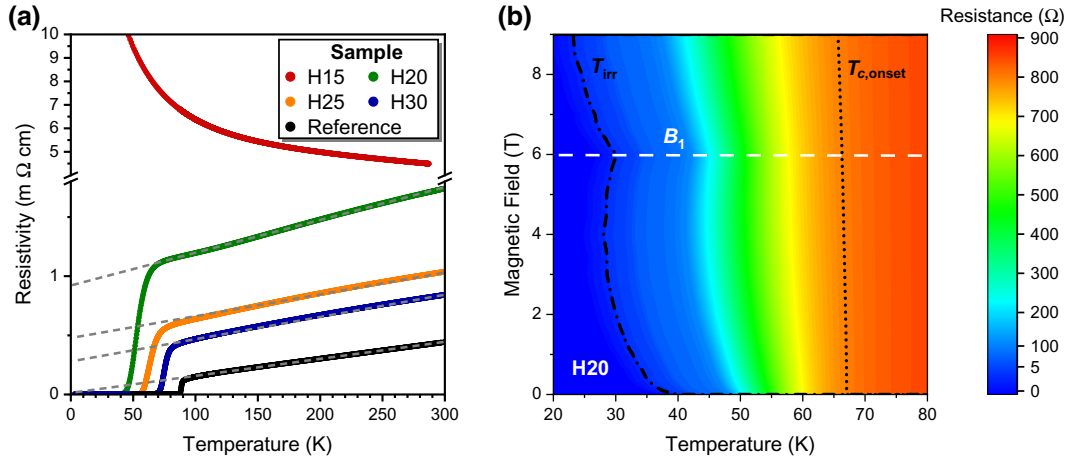
FIG. 5.   (a) Resistivity versus temperature (at $B = 0$) of YBCO microbridges patterned with a hexagonal array of CDs of various spacings a by He-FIB irradiation with dose $D = 10$ ki/dot. Extrapolations of the normal-state resistivities are shown by dashed lines. The black line shows the data of a nonirradiated reference film. (b) Color-coded contour plot of the resistance of sample H20 as a function of temperature and magnetic field. The dotted line represents the onset of superconductivity, $T_{c,\mathrm{onset}}$, taken as 90% of the normal-state resistance value at 100 K, $R(100\ \mathrm{K})$. The dashed-dotted line estimates the irreversibility line T_{irr}, using a criterion of 0.1% of $R(100\ \mathrm{K})$.

decreases with increasing D, the data were taken at the same normalized $T/T_c \sim 0.96$. Although commensurability effects are barely visible at $D = 1$ ki/dot, they appear at higher doses. Still, the $\rho(B)$ curves of the bridges with $D \leq 3.5$ ki/dot are similar and do not show matching dips at B_2. Only for $D = 10$ ki/dot is there a clear matching effect at B_2, and, moreover, the minimum at B_1 is remarkably pronounced. These experimental results confirm the simulation results presented in Fig. 2(b) and point to an optimal dose $D = 10$ ki/dot for our experiments.

2. Spot control

The SC value specifies the strength of the HIM's condenser lens, thus setting the position of the crossover point in the ion optical column. For a given aperture diameter, a higher SC value thus produces a narrower beam profile at the expense of lower ion fluence and longer irradiation time. For SC = 5 used in this study we estimate a beam diameter of FWHM $\varnothing \approx 9$ nm on the sample surface. At a dose of 10 ki/dot the dwell time of the beam for a single spot is about 3 ms, and the total irradiation time of the bridge is approximately 40 min for the lattice spacing $a = 30$ nm.

The processing time can be reduced by a factor of about 2 using SC = 4. To test the consequences, the resistivities at 86.5 K are compared as a function of the applied magnetic field in Fig. 4(b). The two bridges with a hexagonal CD pattern of $a = 40$ nm were manufactured from the same YBCO film and treated identically, except for the choice of SC. Despite the similarity of the vortex-matching characteristics, the resistivity of the SC = 4 bridge is

higher due to a wider tail of the ion beam profile, resulting in a higher defect density between the irradiated spots.

B. Resistivity and critical current

The microbridges described in Table I were further studied by electrical transport measurements. Figure 5(a) depicts the resistivity $\rho(T)$ of all four microbridges with arrays written using $D = 10$ ki/dot together with a nonirradiated reference film. The samples with $A = 30$, 25, and 20 nm exhibit a metallic temperature dependence in the normal state and a critical temperature that decreases with smaller spacing. An invariance of the slope indicates that no oxygen is lost during irradiation [33], while the rising offset of a straight line extrapolated from the normal state indicates an increase in the number of defects in the percolation paths between the CDs. This observation is consistent with the decline of T_c and the simulation results presented in Fig. 2(a).

In contrast, the array with $a = 15$ nm displays a semiconducting $\rho(T)$ dependence and does not become superconducting even at our lowest measurement temperature of 2 K. When the CDs are placed at such a close spacing, they begin to overlap and impede the supercurrent between the CDs. This observation from the resistivity measurements for variable a supports our estimate of the He-FIB's fluence profile $\varnothing = 9$ nm in the simulations.

In order to further investigate the superconducting transition of sample H20, we measured $R(T)$ for different magnetic fields, as shown in Fig. 5(b). The dotted line represents the onset of superconducting percolation paths between the CDs, $T_{c,\mathrm{onset}}(B)$, which is defined as $R(T_{c,\mathrm{onset}}, B) = 0.9R(100\ \mathrm{K}, B)$. The steep slope
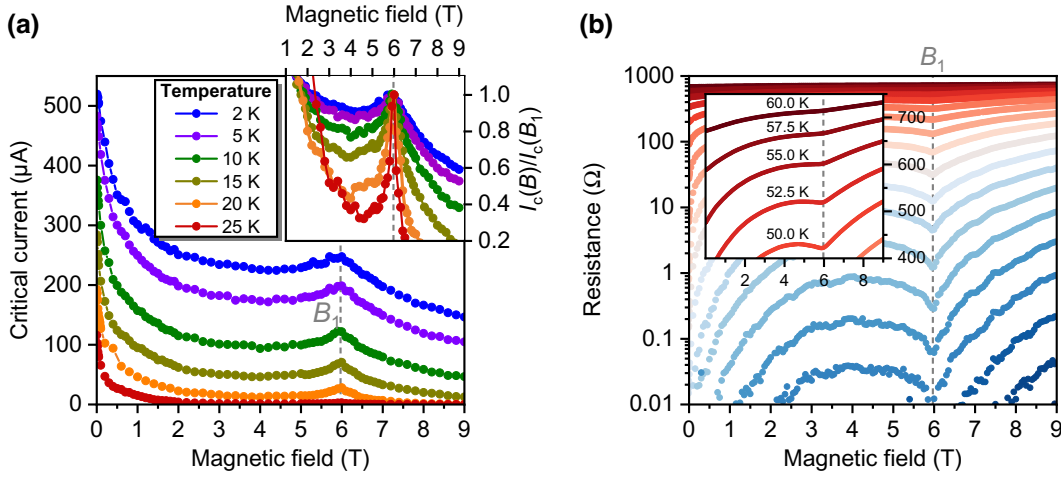
FIG. 6. Effects of vortex commensurability in sample H20. (a) Critical current versus applied magnetic field at various temperatures. The inset shows the critical current normalized to its value at the matching field B_1. (b) Resistance versus applied magnetic field at temperatures from 17.5 K (dark blue symbols) to 60 K (dark red symbols) in 2.5 K steps. The inset shows details at higher temperatures.

$-dB/dT_{c,\mathrm{onset}}$ implies that the upper critical field $B_{c2}(0\,\mathrm{K})$ is very high. Remarkably, no features in $T_{c,\mathrm{onset}}(B)$ are observed at the first matching field $B_1 = 6.0$ T [horizontal dashed line in Fig. 5(b)]. This suggests that in the strong fluctuation and vortex liquid regime near $T_{c,\mathrm{onset}}(B)$, the current paths between the CDs are basically unaffected by the pinning array and the slope of $T_{c,\mathrm{onset}}(B)$ is comparable to that of nonirradiated films. In contrast, we observe a distinct peak of the irreversibility temperature $T_{\mathrm{irr}}(B)$, defined as $R(T_{\mathrm{irr}}, B) = 10^{-3}R(100\,\mathrm{K}, B)$, right at B_1. This indicates that the onset of dissipation caused by moving vortices is significantly shifted to higher temperatures when the vortices can arrange themselves commensurably with the CD array.

The vortex-matching effects can be investigated more directly by critical current $I_c(B)$ (static probe) or resistance $R(B)$ (dynamic property of moving vortices) measurements. The $I_c(B)$ curves in Fig. 6(a), taken at six different temperatures from 2 to 25 K, show peaks at $B_1 = 6.0$ T, which remain visible even down to $T = 2$ K. The inset of the figure highlights these peaks by normalizing I_c to $I_c(B_1)$. As the temperature increases, the pinning force of intrinsic defects decreases faster than that of CDs [42], which makes the peaks even more pronounced. It is worth noting that previous works [16–18,23,25–27,34,43–49] did not identify commensurability effects at such high magnetic fields. Furthermore, the vortex matching observed in our samples continues to occur even at very low temperatures. These observations are a natural consequence of ultradense and strong pinning sites created by He-FIB irradiation.

From Fig. 6(a) it is evident that the pinning effect remains strong not only at B_1 but also throughout the field range $0 \leq B < B_1$, where commensurability effects are less significant. The minimum value of I_c, which roughly

corresponds to the weakest pinning sites, is reached at about 4 T at low temperatures. At the lowest temperature $T = 2$ K, $I_c(B = 4\,\mathrm{T})$ is only half the value of $I_c(B = 0)$. However, for $B > B_1$ the pinning becomes less effective and I_c decays more rapidly. While at $B < B_1$ every vortex can, in principle, be pinned solely in a CD, this is not the case for $B > B_1$. Then an arrangement of multiquantum vortices in the CDs or interstitial vortices occurs, which is energetically less favorable. Thus, the value of B_1 sets an upper limit to the typical range of strong pinning that is relevant for practical applications. This implies that shifting B_1 to high magnetic fields is essential, which is possible with the method presented here.

On the high-temperature side, up to about 60 K, the vortex-matching effects are probed via reduced vortex mobility, resulting in minima of the resistance as shown in Fig. 6(b). This suggests that even at 80% of the normal-state resistance value $R(100\,\mathrm{K})$, correlations between vortices do exist. Hence, the vortex ensemble is not entirely melted but instead moves through a plastic vortex flow [50]. Voltage-current isotherms in sample H30 indicate that the interaction of artificial and intrinsic defects results in an ordered Bose glass state [51,52].

The magnetoresistance of sample H20 was investigated up to 12.5 T in a separate series of measurements. Figure 7 shows the $R(B)$ curves at temperatures from 17 to 55 K. Some measurements were taken at both magnetic field polarities to confirm the perfect mirror symmetry of the data. We do not find matching features [dips in $R(B)$] at $B_2 = 12.0$ T, though minima in $R(B)$ at B_2 are visible for the H30 bridge with a wider hexagonal $a = 30$ nm CD array [see Fig. 4(a)]. In addition, $I_c(B)$, measured on the H20 bridge at lower temperatures, did not reveal any commensurability signatures at B_2. One possible explanation is that the dynamics of interstitial vortices
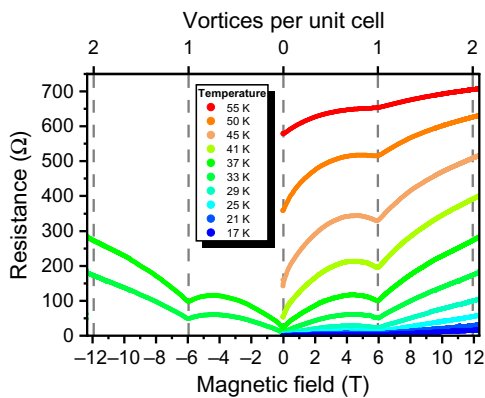
FIG. 7. Resistance versus applied magnetic field at various temperatures of the YBCO microbridge H20 patterned with a hexagonal array of CDs (spacing $a = 20$ nm and dose $D = 10$ ki/dot). Some data were collected in both polarities of the magnetic field and confirm the symmetry $R(B) = R(-B)$.

changes when the channels between the CDs become narrow. Such details of vortex-matching properties in ultradense pinning landscapes deserve further investigation.

V. CONCLUSIONS

To summarize, irradiating thin YBCO films with a 30-keV focused helium ion beam of undercritical dose $D < D_c$ is an excellent approach for introducing user-defined patterns of suppressed critical temperature. After evaluating the appropriate irradiation conditions, we demonstrated the ability to create ultradense hexagonal pinning arrays with a spacing as low as $a = 20$ nm. These arrays exhibit strong pinning across a wide range of magnetic fields up to the first matching field of 6 T. The overlap of neighboring CDs sets the present experimental minimum separation of the pins at 15 nm $< a \leq 20$ nm. However, it is possible that further adjustment of irradiation parameters could slightly reduce this constraint.

Our experiments have shown that vortex-matching effects can be observed even at low temperatures of 2 K, where superconductivity is stable and not affected by fluctuations. This paves the way for designing more effective pinning landscapes that can operate at several tesla and at temperatures much lower than the critical temperature, avoiding the undesirable vortex liquid and fluctuation regimes.

Our findings have expanded the range of temperatures and magnetic fields that can be studied with *regular* artificial pinning landscapes. In order to bring the theoretical concepts in the field of fluxonics [6,8,10,11] into practical use and to facilitate high operating frequencies, it is essential to confine vortices to designed features with the smallest possible size [9]. With our findings, it is now possible to create complex pinning patterns with narrow spacing that can be utilized in applications such as

vortex-based cellular automata for fast logic with low power consumption [9,10]. Future developments in He-FIB instrumentation, such as a multibeam technique [53], would further augment the versatility of the presented method.

ACKNOWLEDGMENTS

[1] G. Blatter, M. V. Feigel'man, V. B. Geshkenbein, A. I. Larkin, and V. M. Vinokur, Vortices in high-temperature superconductors, Rev. Mod. Phys. **66**, 1125 (1994).

[2] J. Pearl, Current distribution in superconducting films carrying quantized fluxoids, Appl. Phys. Lett. **5**, 65 (1964).

[3] C. Sekirnjak, W. Lang, S. Proyer, and P. Schwab, Novel approach for the analysis of the fluctuation magnetoconductivity in YBa$_2$Cu$_3$O$_7$ thin films, Physica C **243**, 60 (1995).

[4] D. Rohner, L. Thiel, B. Müller, M. Kasperczyk, R. Kleiner, D. Koelle, and P. Maletinsky, Real-space probing of the local magnetic response of thin-film superconductors using single spin magnetometry, Sensors **18**, 3790 (2018).

[5] M. J. Martínez-Pérez, B. Müller, D. Schwebius, D. Korinski, R. Kleiner, J. Sesé, and D. Koelle, NanoSQUID magnetometry of individual cobalt nanoparticles grown by focused

electron beam induced deposition, Supercond. Sci. Technol. – Focus Issue on NanoSQUIDs and Their Applications **30,** 024003 (2017).

[6] T. Golod, A. Iovan, and V. M. Krasnov, Single Abrikosov vortices as quantized information bits, Nat. Commun. **6,** 8628 (2015).

[7] I. Keren, A. Gutfreund, A. Noah, N. Fridman, A. Di Bernardo, H. Steinberg, and Y. Anahory, Chip-integrated vortex manipulation, Nano Lett. **23,** 4669 (2023).

[8] J. F. Wambaugh, C. Reichhardt, C. J. Olson, F. Marchesoni, and F. Nori, Superconducting fluxon pumps and lenses, Phys. Rev. Lett. **83,** 5106 (1999).

[9] M. B. Hastings, C. J. Olson Reichhardt, and C. Reichhardt, Ratchet cellular automata, Phys. Rev. Lett. **90,** 247004 (2003).

[10] M. V. Milošević, G. R. Berdiyorov, and F. M. Peeters, Fluxonic cellular automata, Appl. Phys. Lett. **91,** 212501 (2007).

[11] T. Golod, L. Morlet-Decarnin, and V. M. Krasnov, Word and bit line operation of a 1×1 μm^2 superconducting vortex-based memory, Nat. Commun. **14,** 4926 (2023).

[12] A. Libál, C. J. Olson Reichhardt, and C. Reichhardt, Creating artificial ice states using vortices in nanostructured superconductors, Phys. Rev. Lett. **102,** 237004 (2009).

[13] J. E. Villegas, S. Savel'ev, F. Nori, E. M. Gonzalez, J. V. Anguita, R. García, and J. L. Vicent, A superconducting reversible rectifier that controls the motion of magnetic flux quanta, Science **302,** 1188 (2003).

[14] Y.-Y. Lyu, J. Jiang, Y.-L. Wang, Z.-L. Xiao, S. Dong, Q.-H. Chen, M. V. Milošević, H. Wang, R. Divan, J. E. Pearson, P. Wu, F. M. Peeters, and W.-K. Kwok, Superconducting diode effect via conformal-mapped nanoholes, Nat. Commun. **12,** 2703 (2021).

[15] J. Trastoy, M. Malnou, C. Ulysse, R. Bernard, N. Bergeal, G. Faini, J. Lesueur, J. Briatico, and J. E. Villegas, Freezing and thawing of artificial ice by thermal switching of geometric frustration in magnetic flux lattices, Nat. Nanotechnol. **9,** 710 (2014).

[16] V. V. Moshchalkov and J. Fritzsche, *Nanostructured Superconductors* (World Scientific, Singapore, 2011).

[17] A. Castellanos, R. Wördenweber, G. Ockenfuss, A. v.d. Hart, and K. Keck, Preparation of regular arrays of antidots in $YBa_2Cu_3O_7$ thin films and observation of vortex lattice matching effects, Appl. Phys. Lett. **71,** 962 (1997).

[18] S. Avci, Z. L. Xiao, J. Hua, A. Imre, R. Divan, J. Pearson, U. Welp, W. K. Kwok, and G. W. Crabtree, Matching effect and dynamic phases of vortex matter in $Bi_2Sr_2CaCu_2O_8$ nanoribbon with a periodic array of holes, Appl. Phys. Lett. **97,** 042511 (2010).

[19] W. Vinckx, J. Vanacken, V. V. Moshchalkov, S. Mátéfi-Tempfli, M. Mátéfi-Tempfli, S. Michotte, and L. Piraux, Vortex pinning in superconducting Nb thin films deposited on nanoporous alumina templates, Eur. Phys. J. B **53,** 199 (2006).

[20] F. Kahlmann, A. Engelhardt, J. Schubert, W. Zander, C. Buchal, and J. Hollkott, Superconductor-normal-superconductor Josephson junctions fabricated by oxygen implantation into $YBa_2Cu_3O_{7-\delta}$, Appl. Phys. Lett. **73,** 2354 (1998).

[21] A. S. Katz, S. I. Woods, and R. C. Dynes, Transport properties of high-T_c planar Josephson junctions fabricated by nanolithography and ion implantation, J. Appl. Phys. **87,** 2978 (2000).

[22] D. J. Kang, G. Burnell, S. J. Lloyd, R. S. Speaks, N. H. Peng, C. Jeynes, R. Webb, J. H. Yun, S. H. Moon, B. Oh, E. J. Tarte, D. F. Moore, and M. G. Blamire, Realization and properties of $YBa_2Cu_3O_{7-\delta}$ Josephson junctions by metal masked ion damage technique, Appl. Phys. Lett. **80,** 814 (2002).

[23] I. Swiecicki, C. Ulysse, T. Wolf, R. Bernard, N. Bergeal, J. Briatico, G. Faini, J. Lesueur, and J. E. Villegas, Strong field-matching effects in superconducting $YBa_2Cu_3O_{7-\delta}$ films with vortex energy landscapes engineered via masked ion irradiation, Phys. Rev. B **85,** 224502 (2012).

[24] W. Lang, M. Dineva, M. Marksteiner, T. Enzenhofer, K. Siraj, M. Peruzzi, J. D. Pedarnig, D. Bäuerle, R. Korntner, E. Cekan, E. Platzgummer, and H. Loeschner, Ion-beam direct-structuring of high-temperature superconductors, Microelectron. Eng. **83,** 1495 (2006).

[25] L. T. Haag, G. Zechner, W. Lang, M. Dosmailov, M. A. Bodea, and J. D. Pedarnig, Strong vortex matching effects in YBCO films with periodic modulations of the superconducting order parameter fabricated by masked ion irradiation, Physica C **503,** 75 (2014).

[26] G. Zechner, F. Jausner, L. T. Haag, W. Lang, M. Dosmailov, M. A. Bodea, and J. D. Pedarnig, Hysteretic vortex-matching effects in high-T_c superconductors with nanoscale periodic pinning landscapes fabricated by He ion-beam projection, Phys. Rev. Appl. **8,** 014021 (2017).

[27] G. Zechner, K. L. Mletschnig, W. Lang, M. Dosmailov, M. A. Bodea, and J. D. Pedarnig, Unconventional critical state in $YBa_2Cu_3O_{7-\delta}$ thin films with a vortex-pin lattice fabricated by masked He^+ ion beam irradiation, Supercond. Sci. Technol. **31,** 044002 (2018).

[28] G. Zechner, W. Lang, M. Dosmailov, M. A. Bodea, and J. D. Pedarnig, Transverse vortex commensurability effect and sign change of the Hall voltage in superconducting $YBa_2Cu_3O_{7-\delta}$ thin films with a nanoscale periodic pinning landscape, Phys. Rev. B **98,** 104508 (2018).

[29] R. L. Gray, M. J. D. Rushton, and S. T. Murphy, Molecular dynamics simulations of radiation damage in $YBa_2Cu_3O_7$, Supercond. Sci. Technol. **35,** 035010 (2022).

[30] S. J. Rothman, J. L. Routbort, and J. E. Baker, Tracer diffusion of oxygen in $YBa_2Cu_3O_{7-\delta}$, Phys. Rev. B **40,** 8852 (1989).

[31] S. K. Tolpygo, J. Y. Lin, M. Gurvitch, S. Y. Hou, and J. M. Phillips, Effect of oxygen defects on transport properties and T_c of $YBa_2Cu_3O_{6+x}$: Displacement energy for plane and chain oxygen and implications for irradiation-induced resistivity and T_c suppression, Phys. Rev. B **53,** 12462 (1996).

[32] W. Lang, H. Richter, M. Marksteiner, K. Siraj, M. A. Bodea, J. D. Pedarnig, C. Grigoropoulos, D. Bäuerle, C. Hasenfuss, L. Palmetshofer, R. Kolarova, and P. Bauer, Masked ion beam irradiation of high-temperature superconductors: Patterning of nano-size regions with high point-defect density, Int. J. Nanotechnol. **6,** 704 (2009).

[33] W. Lang and J. D. Pedarnig, Ion irradiation of high-temperature superconductors and its application for nanopatterning, in *Nanoscience and Engineering in Superconductivity*, edited by V. V. Moshchalkov, R. Wördenweber, and W. Lang (Springer, Berlin, 2010), p. 81.

[34] C. Yang, H. Liu, Y. Liu, J. Wang, D. Qiu, S. Wang, Y. Wang, Q. He, X. Li, P. Li, Y. Tang, J. Wang, X. C. Xie, J. M. Valles, J. Xiong, and Y. Li, Signatures of a strange metal in a bosonic system, Nature **601,** 205 (2022).

[35] *Helium Ion Microscopy*, edited by G. Hlawacek and A. Gölzhäuser (Springer International Publishing, Cham, 2016).

[36] D. Niebieskikwiat, A. Silhanek, L. Civale, G. Nieva, P. Levy, and L. Krusin-Elbaum, Suppression of matching field effects by splay and pinning energy dispersion in $YBa_2Cu_3O_7$ with columnar defects, Phys. Rev. B **63,** 144504 (2001).

[37] S. A. Cybart, E. Y. Cho, T. J. Wong, B. H. Wehlin, M. K. Ma, C. Huynh, and R. C. Dynes, Nano Josephson superconducting tunnel junctions in $YBa_2Cu_3O_{7-\delta}$ directly patterned with a focused helium ion beam, Nat. Nanotechnol. **10,** 598 (2015).

[38] B. Müller, M. Karrer, F. Limberger, M. Becker, B. Schröppel, C. J. Burkhardt, R. Kleiner, E. Goldobin, and D. Koelle, Josephson junctions and SQUIDs created by focused helium-ion-beam irradiation of $YBa_2Cu_3O_7$, Phys. Rev. Appl. **11,** 044082 (2019).

[39] J. F. Ziegler, M. D. Ziegler, and J. P. Biersack, SRIM – the stopping and range of ions in matter (2010), Nucl. Instrum. Methods Phys. Res., Sect. B **268,** 1818 (2010).

[40] K. L. Mletschnig and W. Lang, Nano-patterning of cuprate superconductors by masked He^+ ion irradiation: 3-dimensional profiles of the local critical temperature, Microelectron. Eng. **215,** 110982 (2019).

[41] A. I. Buzdin, Multiple-quanta vortices at columnar defects, Phys. Rev. B **47,** 11416 (1993).

[42] I. B. Khalfin and B. Y. Shapiro, Relaxation of magnetic flux in a superconductor with a system of columnar defects, Physica C **207,** 359 (1993).

[43] J. Y. Lin, M. Gurvitch, S. K. Tolpygo, A. Bourdillon, S. Y. Hou, and J. M. Phillips, Flux pinning in $YBa_2Cu_3O_{7-\delta}$ thin films with ordered arrays of columnar defects, Phys. Rev. B **54,** R12717 (1996).

[44] R. Córdoba, T. I. Baturina, J. Sesé, A. Y. Mironov, J. M. de Teresa, M. R. Ibarra, D. A. Nasimov, A. K. Gutakovskii, A. V. Latyshev, I. Guillamón, H. Suderow, S. Vieira, M. R. Baklanov, J. J. Palacios, and V. M. Vinokur, Magnetic field-induced dissipation-free state in superconducting nanostructures, Nat. Commun. **4,** 1437 (2013).

[45] N. Poccia, T. I. Baturina, F. Coneri, C. G. Molenaar, X. R. Wang, G. Bianconi, A. Brinkman, H. Hilgenkamp, A. A. Golubov, and V. M. Vinokur, Critical behavior at a dynamic vortex insulator-to-metal transition, Science **349,** 1202 (2015).

[46] I. G. Serrano, J. Sesé, I. Guillamón, H. Suderow, S. Vieira, M. R. Ibarra, and J. M. de Teresa, Thickness-modulated tungsten–carbon superconducting nanostructures grown by focused ion beam induced deposition for vortex pinning up to high magnetic fields, Beilstein J. Nanotechnol. **7,** 1698 (2016).

[47] O. V. Dobrovolskiy, V. M. Bevz, M. Y. Mikhailov, O. L. Yuzephovich, V. A. Shklovskij, R. V. Vovk, M. I. Tsindlekht, R. Sachser, and M. Huth, Microwave emission from superconducting vortices in Mo/Si superlattices, Nat. Commun. **9,** 4927 (2018).

[48] B. Aichner, B. Müller, M. Karrer, V. R. Misko, F. Limberger, K. L. Mletschnig, M. Dosmailov, J. D. Pedarnig, F. Nori, R. Kleiner, D. Koelle, and W. Lang, Ultradense tailored vortex pinning arrays in superconducting $YBa_2Cu_3O_{7-\delta}$ thin films created by focused He ion beam irradiation for fluxonics applications, ACS Appl. Nano Mater. **2,** 5108 (2019).

[49] C. Yang, Y. Liu, Y. Wang, L. Feng, Q. He, J. Sun, Y. Tang, C. Wu, J. Xiong, W. Zhang, X. Lin, H. Yao, H. Liu, G. Fernandes, J. Xu, J. M. Valles, J. Wang, and Y. Li, Intermediate bosonic metallic state in the superconductor-insulator transition, Science **366,** 1505 (2019).

[50] C. Reichhardt and C. J. Olson Reichhardt, Depinning and nonequilibrium dynamic phases of particle assemblies driven over random and ordered substrates: A review, Rep. Prog. Phys. **80,** 026501 (2017).

[51] L. Backmeister, B. Aichner, M. Karrer, K. Wurster, R. Kleiner, E. Goldobin, D. Koelle, and W. Lang, Ordered Bose glass of vortices in superconducting $YBa_2Cu_3O_{7-\delta}$ thin films with a periodic pin lattice created by focused helium ion irradiation, Nanomaterials **12,** 3491 (2022).

[52] B. Aichner, L. Backmeister, M. Karrer, K. Wurster, R. Kleiner, E. Goldobin, D. Koelle, and W. Lang, Angle-dependent magnetoresistance of an ordered Bose glass of vortices in $YBa_2Cu_3O_{7-\delta}$ thin films with a periodic pinning lattice, Condens. Matter **8,** 32 (2023).

[53] K. Höflich, *et al.*, Roadmap for focused ion beam technologies, Appl. Phys. Rev. **10,** 041311 (2023).